The Astrophysical Journal, 784:1 (15pp), 2014 March 20 doi:10.1088/0004-637X/784/1/1

SHOCKS AND STAR FORMATION IN STEPHAN'S QUINTET. I. GEMINI SPECTROSCOPY OF Hα-BRIGHT KNOTS

I. S. Konstantopoulos[1,11], P. N. Appleton[2], P. Guillard[3], G. Trancho[4], M. E. Cluver[1], N. Bastian[5], J. C. Charlton[6], K. Fedotov[7,8], S. C. Gallagher[7], L. J. Smith[9], and C. J. Struck[10]
[1] Australian Astronomical Observatory, P.O. Box 915, North Ryde NSW 1670, Australia; iraklis@aao.gov.au
[2] NASA Herschel Science Center (NHSC), California Institute of Technology, Pasadena, CA 91125, USA
[3] Institut d'Astrophysique Spatiale, Université Paris-Sud XI, F-91405 Orsay, Cedex, France
[4] Giant Magellan Telescope Organisation, Pasadena, CA 91101, USA
[5] Astrophysics Research Institute, Liverpool John Moores University, Liverpool L3 5RF, UK
[6] Department of Astronomy and Astrophysics, The Pennsylvania State University, University Park, PA 16802, USA
[7] Department of Physics and Astronomy, The University of Western Ontario, London, ON N6A 3K7, Canada
[8] Herzberg Institute of Astrophysics, Victoria BC, V9E 2E7, Canada
[9] Space Telescope Science Institute and European Space Agency, Baltimore, MD 21218, USA
[10] Department of Physics and Astronomy, Iowa State University, Ames, IA 50011, USA
Received 2013 October 16; accepted 2013 November 27; published 2014 February 25

ABSTRACT

We present a Gemini-GMOS spectroscopic study of *Hubble Space Telescope* (*HST*)-selected Hα-emitting regions in Stephan's Quintet (HCG 92), a nearby compact galaxy group, with the aim of disentangling the processes of shock-induced heating and star formation in its intra-group medium. The ≈40 sources are distributed across the system, but most densely concentrated in the ∼kiloparsec-long shock region. Their spectra neatly divide them into narrow- and broad-line emitters, and we decompose the latter into three or more emission peaks corresponding to spatial elements discernible in *HST* imaging. The emission-line ratios of the two populations of Hα-emitters confirm their nature as H II regions (90% of the sample) or molecular gas heated by a shock front propagating at $\lesssim$300 km s^{-1}. Their redshift distribution reveals interesting three-dimensional structure with respect to gas-phase baryons, with no H II regions associated with shocked gas, no shocked regions in the intruder galaxy NGC 7318B, and a sharp boundary between shocks and star formation. We conclude that star formation is inhibited substantially, if not entirely, in the shock region. Attributing those H II regions projected against the shock to the intruder, we find a lopsided distribution of star formation in this galaxy, reminiscent of pileup regions in models of interacting galaxies. The Hα luminosities imply mass outputs, star formation rates, and efficiencies similar to nearby star-forming regions. Two large knots are an exception to this, being comparable in stellar output to the prolific 30 Doradus region. We also examine Stephan's Quintet in the context of compact galaxy group evolution, as a paradigm for intermittent star formation histories in the presence of a rich, X-ray-emitting intra-group medium. All spectra are provided as supplemental materials.

Key words: galaxies: groups: individual (HCG 92) – galaxies: individual (NGC 7317, NGC 7318A, NGC 7318B, NGC 7319) – galaxies: interactions – galaxies: star formation – intergalactic medium – shock waves

Online-only material: color figures, FITS files

1. INTRODUCTION

The interplay between shocks and the collapse of gaseous material into stars is as yet not fully understood. While shock fronts are conspicuously observed to propagate through star-forming regions after the first generation of supernova explosions (following the "triggering" paradigm set by Elmegreen & Lada 1977), one might expect the net effect to be the suppression star formation, as the shock comes with a deposition of energy that should heat up the interstellar medium (such as the strong shocks studied by Reynaud & Downes 1998). An extra complication is the contemporaneous presence of turbulent flows in star-forming regions. At the molecular core level, several models have long advocated turbulence as the dominant collapse mechanism in the interstellar medium (e.g., Elmegreen 2002; Klessen & Hennebelle 2010; Nakamura & Li 2011, and many others), and have gained support from the recent observations of a correlation between H I line broadening above the thermal value, attributed to turbulence, and the local star formation rate (SFR; Tamburro et al. 2009, based on a sample of ≈30 nearby galaxies). However, the opposing side argues that turbulence tends to inhibit the process in various ways, e.g., by inducing runaway collapse when acting as the only gravitational agent (Hopkins et al. 2011), or that such "local viscosity" is dwarfed by the effect of global torques (Thompson et al. 2005). Other models have demonstrated an indifference on the part of star formation to the effects of triggering by turbulence (most notably Dale et al. 2007; Getman et al. 2012). Finally, while shocks and turbulence are spatially correlated with star formation, an argument was recently made by Mac Low (2013) against any form of causality: newborn stars may simply be riding in the same carriage as turbulence and shocks. In this scenario, gravitational instabilities are enough to drive star formation, with no need for other input physics.

From the above it is clear that the conjunction of these energy input mechanisms is very difficult to interpret in observations and modeling of highly extinguished, nearby star-forming regions. With no clear tipping of the scales in favor of shocks, turbulence, radiation pressure, cooling (Bonnell et al. 2013), magnetic fields (Sellwood & Balbus 1999), and all other

[11] Recipient of a John Stocker Postdoctoral Fellowship from the Science and Industry Research Fund.

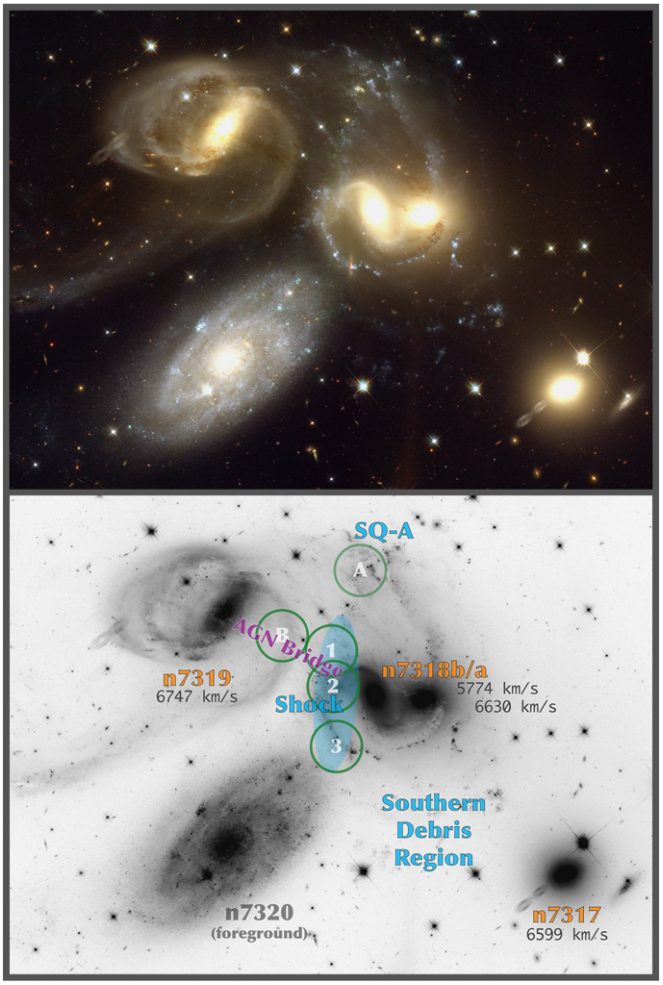

Figure 1. Optical imaging (*BVI*-equivalent, top) and annotated grayscale (bottom) map of Stephan's Quintet (HCG 92). North is to the top and east to the left, and the image spans approximately 5′, or 120 kpc at the adopted distance of 94 Mpc. We mark the four galaxies that form the core of the group and their velocities (a fifth galaxy, NGC 7320C lies to the northeast), a foreground spiral, and four regions of interest: the shock front (pale blue), the southern debris region, X-ray emitter SQ-A, and the "AGN bridge" (see text for information on these regions and related bibliography). Green circles represent the CO pointings of Guillard et al. (2012).

(A color version of this figure is available in the online journal.)

mechanisms proposed in the literature, perhaps these potential effects are best studied one at a time. Strong shocks are more common in extra-galactic environments, where friction and collisions can shock-heat large volumes of gas. One of the strongest shock regions in the local universe can be found in the site of the high-speed collision between NGC 7318B and the intra-group medium (IGM) of Stephan's Quintet to which we will sometimes refer as "the Quintet"; see Figure 1), a nearby compact galaxy group (CG; $u_R = 6600$ km s^{-1}, $d = 94$ Mpc if $H_0 = 70$ km s^{-1} Mpc^{-1}). The high luminosity of the X-ray emission ($L_X = 4 \times 10^{41}$erg s^{-1}; Sulentic et al. 1995) is rather inviting for various investigations not only into the role of shocks as agents of star formation, but also the evolution of galaxy groupings. While the Quintet does not lack the mass required to heat up its IGM, collisions might be the only way to develop an X-ray medium for low-mass compact groups. In this scenario, however, maintaining such an IGM temperature is conditional on consequent collisions and therefore on a continuing association with the interloper (as an upper limit, the gas cools within ∼1 Gyr in the simulations of Hwang et al. 2012). This way a fraction of the IGM can become locked in this hot phase for long and take away a potentially significant part of the reservoir of gas available for star formation. A high-speed collision is then a crucial event in the history of a CG, defining one potential evolutionary pathway that relies on the presence of an IGM (one of the two sequences described by Konstantopoulos et al. 2010). If that is the case, then it is worth asking how much gas can get enveloped in such an event, and how does this heat capacity relate to the suppression of star formation on a group-wide scale?

In the Quintet, Appleton et al. (2006) and Cluver et al. (2010) mapped the intensity of the warm infrared H_2 transition and established this as the dominant cooling pathway in a molecular medium that seems to be forming stars rather inefficiently. This low star formation efficiency (SFE) has also been deduced with UV, optical, and IR imaging, with Xu et al. (2005) reporting a SFR $= 6.7\ M_\odot$ yr^{-1}, of which 30% can be attributed to the bright starburst region known as SQ-A (or the northern starburst region), which is thought to have resulted from an interaction between the intruder and NGC 7318B, taking place before the collision that shocked the IGM (Renaud et al. 2010; Hwang et al. 2012). However, much of the UV flux on which this SFR measurement is based may be arising from shock excitation lines instead of photoionization. Context for this SFR is provided by the submillimeter observations by Guillard et al. (2012) and others (Yun 1997; Verdes-Montenegro et al. 1998; Leon et al. 1998; Gao & Xu 2000; Smith & Struck 2001; Petitpas & Taylor 2005), who have accounted for the presence of $\approx 4 \times 10^9\ M_\odot$ of cool H_2 in the shock region. The interpretation on offer is a turbulent cascade process that injects energy within the molecular gas so that its turbulent energy becomes comparable to or higher than its gravitational energy (most of the gas is found to be not only warm, but also diffuse; Guillard et al. 2012; Appleton et al. 2013). This establishes a causal relation, whereby shocks heat the medium and therefore inhibit the collapse of gas into stars. In this context, the onset, propagation, and energy deposition by shocks is a central piece of the galaxy evolution puzzle, whenever arrangements such as the Quintet come about.

Conversely, however, if the number of bright, compact, blue sources is a testament to the current state of star formation and its recent history, then the strong shock does not appear to be largely inhibiting the collapse of molecular clouds into stars. The studies of Gallagher et al. (2001) and Fedotov et al. (2011) used *Hubble Space Telescope* (*HST*) imaging to identify hundreds of star clusters and associations across the shock, SQ-A, and elsewhere, and charted the recent interaction history of this complex system. In terms of shocks, while the X-ray-emitting SQ-A is found to host more star clusters than the shock region, the discrepancy may be due to a longer star formation history, rather than a stronger burst. This was, alas, just beyond the diagnostic reach of past *HST*-based studies—although the addition of *U*-band would enable such an investigation. Many results have also been drawn from spectroscopic studies of the Quintet. Trancho et al. (2012) targeted compact sources in the shock, the star-forming bow and debris region south of NGC 7318A, as well as the young tidal tail extending to the east of NGC 7319. In this tail they found a massive, compact cluster of mass $\sim 10^6\ M_\odot$. Their finding of enhanced metallicity for young and currently forming star clusters and associations in the Stephan's Quintet debris system is countered by that of low metallicity gas and stars in the shock region by Iglesias-Páramo et al. (2012).

Table 1
Journal of Science Observations for GMOS-N Program GN-2010B-Q-56

Date	Frame ID	t_{exp} (s)	λ_c (Å)
Mask 1			
2010 Sep 03	N20100903S0103	3130	5900
2010 Sep 03	N20100903S0104	3130	5950
2010 Sep 03	N20100903S0109	3130	5900
2010 Sep 03	N20100903S0110	3130	5950
2010 Sep 06	N20100906S0092	3130	5950
Mask 2			
2010 Sep 03	N20100903S0115	3130	5950
2010 Sep 04	N20100904S0148	3130	5900
2010 Sep 04	N20100904S0149	3130	5950
2010 Sep 04	N20100904S0154	3130	5900
2010 Sep 04	N20100904S0155	3130	5950
Mask 3			
2010 Sep 05	N20100905S0146	3130	5950
2010 Sep 05	N20100905S0151	3130	5900
2010 Sep 05	N20100905S0152	3130	5950
2010 Sep 05	N20100905S0157	3130	5900
2010 Sep 05	N20100905S0158	3130	5950
Mask 4			
2010 Sep 06	N20100906S0085	900	5900
2010 Sep 06	N20100906S0088	900	5950

These two sets of evidence support contrasting interpretations of the role this shock is playing in either suppressing or advancing the formation of new stars. In this paper we present spectroscopy of some ≈40 Hα-emitting knots across the Quintet (in the shock region, SQ-A, and the southern debris region, hereafter SDR), selected from *HST*-Hα images, to help us investigate the link between the large-scale shocks and star formation. We make use of the remarkable wealth of existing broadband coverage and add a much-needed element of spatial resolution. By focusing on spectroscopy we gain access to the velocity axis and can associate these knots with different parts of the complex distribution of the multi-phase gas in the Quintet. Given the broad spatial extent of the hot IGM we examine how any stars can form in this shock region at all, even at a low rate or efficiency. Section 2 describes the data acquisition and reduction effort. In Section 3 we present our spectral line fitting techniques, including Lick indices and multi-component fitting of broad-line spectra. We discuss our findings in Sections 4 and 5, and summarize our interpretation and contribution to the understanding of this well-studied system in Section 6.

2. OBSERVATIONS AND DATA REDUCTION

This work is based on new spectroscopy taken with Gemini GMOS-N in multi-slit mode as part of program GN-2010B-Q-56 (PI: Konstantopoulos), observed in 2010 September under good conditions (typical seeing 0.″8). The spatial coverage is densest in the shock region, however, we sample the rest of the system quite well, with targets in the SDR, SQ-A (Xu et al. 1999), and the "active galactic nucleus (AGN) bridge" between the intruder, NGC 7318B, and NGC 7319 (a broad-line excitation molecular region connecting the two galaxies in projection; Cluver et al. 2010). A full journal of observations can be found in Table 1, while Figures 2–4 mark all observed sources on color-composite *HST*/WFC3 imaging (PID 11502, PI Noll) focused on the shock region, SDR, and SQ-A, respectively. The red–green–blue (RGB) filters correspond to F814W, F606W, and F438W.

Four multi-slit masks were designed using `GMMPS`, the Gemini mask making software, to target sources selected manually on the *HST*-F665N imaging. The 100 Å bandpass transmits all velocities expected in the system. It reaches ≈8100 km s^{-1}, albeit the transmission decreases rapidly above ≈6715 km s^{-1}. We used a brightness criterion for filtering sources, and then accommodated as many as possible on three masks. The fourth mask was designed to target three of the five main galaxies in the Quintet: NGC 7317, NGC 7318A, and NGC 7319, a Seyfert 2 galaxy (Véron-Cetty & Véron 2006). Slitlets were cut to a 0.″75 width while lengths were customized between ≈5″ and 10″ to best accommodate the knots and sufficient background for local sky subtraction. We used the R831 (G5302) grating, which disperses to 0.38 Å pixel^{-1} ($R \approx 4500$). In order to eliminate the inter-chip gaps of the GMOS-N detector, frames were split up into two groups of slightly differing central wavelength: 5900 Å and 5950 Å. Flat field and arc frames bracketed each science exposure to account for detector flexures and any other variant effects (e.g., temperature changes) over the course of each individual exposure. Pixels were binned in the spatial direction without loss of resolution, given the pixel size of ≈0.″07. There was no binning along the spectral axis to preserve resolution.

The spectroscopic data were reduced with a custom pipeline, built around the standard Gemini-IRAF[12] reduction process for GMOS-N. After reducing the image frames with `gsreduce`, offsets were recorded with `gscut` between the bottom of each image and the lower boundary of the first slit. After this registration process we employed `mosproc` in two runs: first to perform bias subtraction and a flat field correction; and then to cut individual slits from each image before extracting and tracing each source in a 1″ aperture, i.e., one resolution element (seeing-limited), regardless of the physical size of the source. This corresponds to roughly 450 pc at the adopted distance of 94 Mpc. At the end of this stage we also produced "clean" images of all frames, useful for qualitative, two-dimensional spectroscopy (see Figure 5). The extraction process (`gsextract`) was first performed on a reference frame, the one that was taken under the best conditions, and the procedure was carbon-copied (with intermediate quality control checks) on all other frames to ensure the application of consistent spectroscopic extraction apertures. The final steps include median-combining all exposures of each spectrum to eliminate chip gaps and cosmic rays, and applying a flux calibration based on a spectroscopic standard star. The above process was then repeated for each mask, before correcting all spectra for foreground extinction from the Milky Way according to the tabulation of Schlegel et al. (1998).

The final, reduced spectra, corrected for foreground extinction, are provided as supplemental materials on the online version of this article. The data set is also available at the following permanent URL: http://dx.doi.org/10.5281/zenodo.7680. The data are provided in the astronomical image transport format, FITS (one file per spectrum), as well as in a single HDF5 (hierarchical data format) file. Some (free) libraries need to be installed to view these files, which can be found on the HDF Group download page, http://www.hdfgroup.org/HDF5/release/obtain5.html. In the HDF5 file the spectra are saved as individual *datasets* of wavelength and flux arrays, and store short, descriptive *attributes*

[12] IRAF is distributed by the National Optical Astronomy Observatory, which is operated by the Association of Universities for Research in Astronomy, Inc., under cooperative agreement with the National Science Foundation.

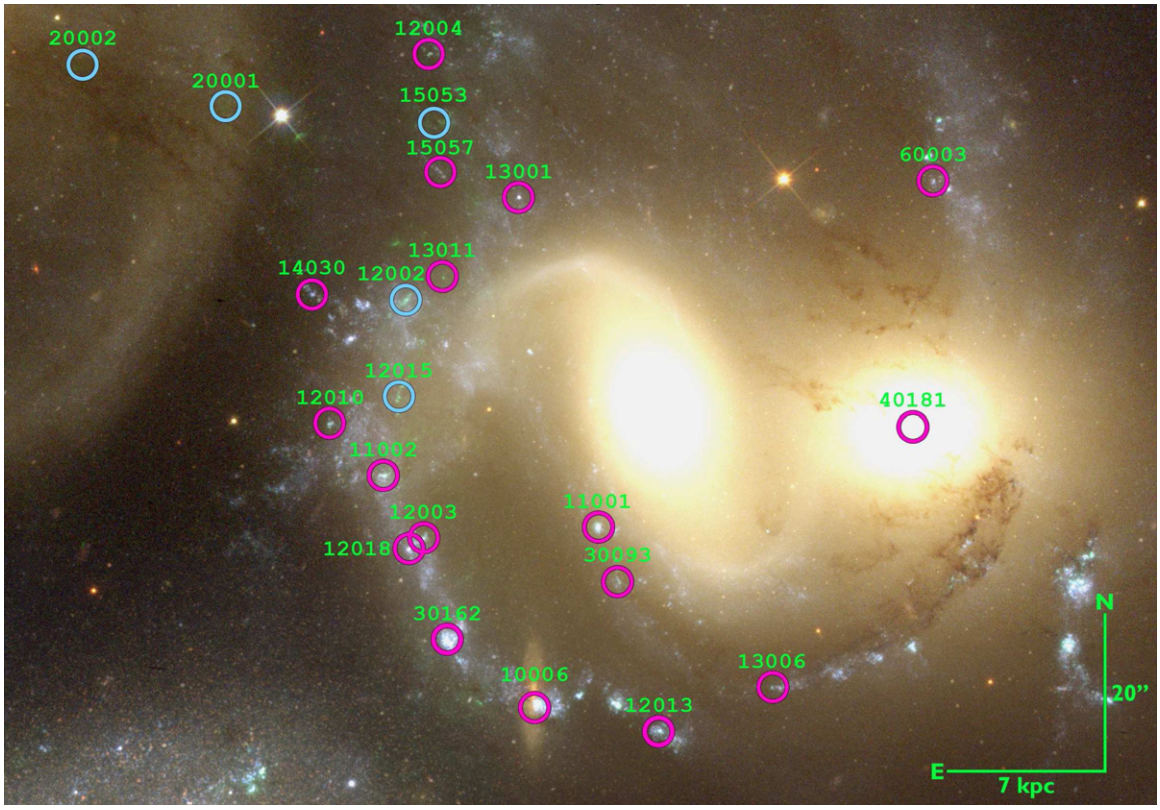

Figure 2. Finding chart showing the approximate placement of spectroscopic slits on archival *HST*/WFC3 imaging. The diameter of the circles corresponds to approximately four times the length of the spectroscopic extraction window, which translates to ≈450 pc at the adopted distance of 94 Mpc. This image, centered on the shock region, is constructed with the F438W, F606W, and F814W images as the blue, green, and red filters. We used narrowband imaging to select targets (F665N), the resolution of which is not matched by our seeing-limited spectroscopic observations. Blue circles denote broad-line sources (see text).

(A color version of this figure is available in the online journal.)

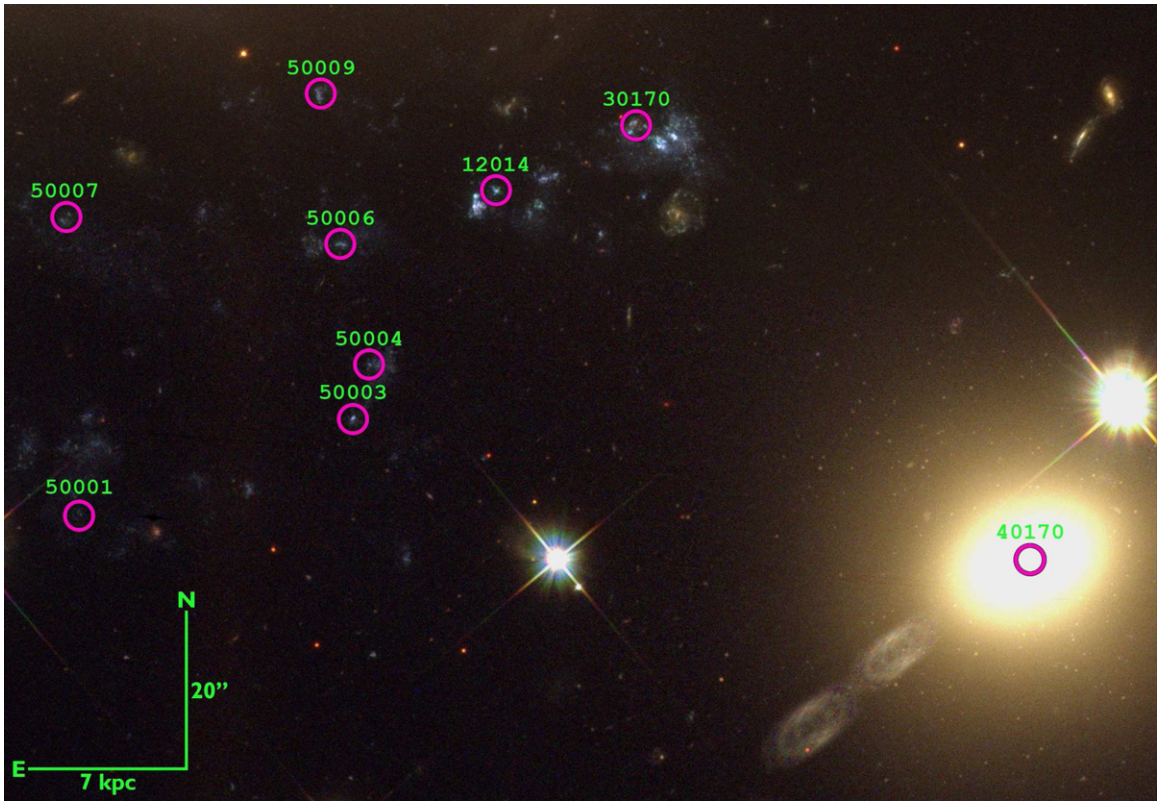

Figure 3. As per Figure 2, for the southern debris region. These targets represent the faintest in our sample, indicating a less massive gaseous reservoir in this region. The artifact resembling the infinity symbol is due to the reflection of the bright star near NGC 7317 (marked as target 40170).

(A color version of this figure is available in the online journal.)

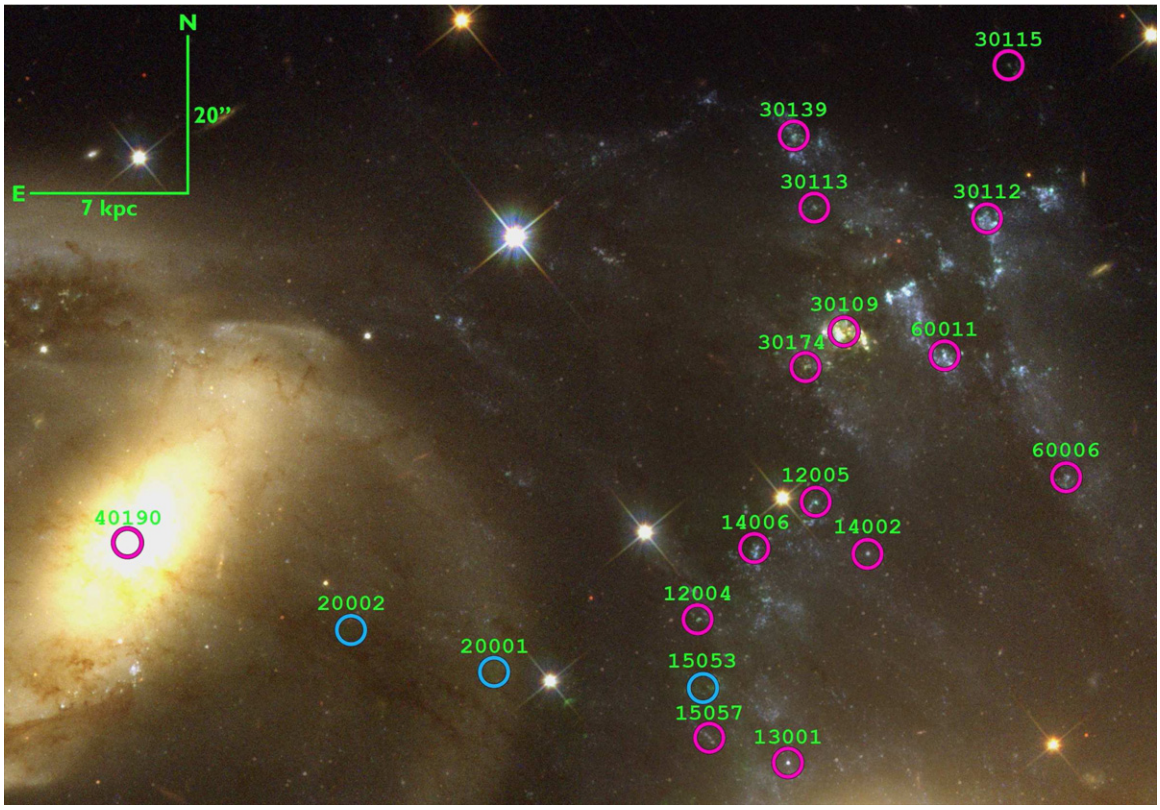

Figure 4. As per Figure 2, for the northern end of the shock region and SQ-A, the bright starburst region to the north of the group core (NGC 7318A/B). We find much nebulosity in SQ-A, following the relatively high local rate of star formation (1.45 $M_{\odot}$ yr^{-1}; Xu et al. 1999). Knots K-30109 and K-30174 have notably yellower colors than the Hα-emitting regions surrounding them, possibly reflecting either higher reddening, or a lower metallicity. The velocity of knot K-30113 pushes it out of the transmission of the employed Hα filter. This finder also covers the "AGN bridge" (Cluver et al. 2010; knots K-20001 and K-20002) leading to NGC 7319 (K-40190). Both "bridge" spectra display broad emission lines.

(A color version of this figure is available in the online journal.)

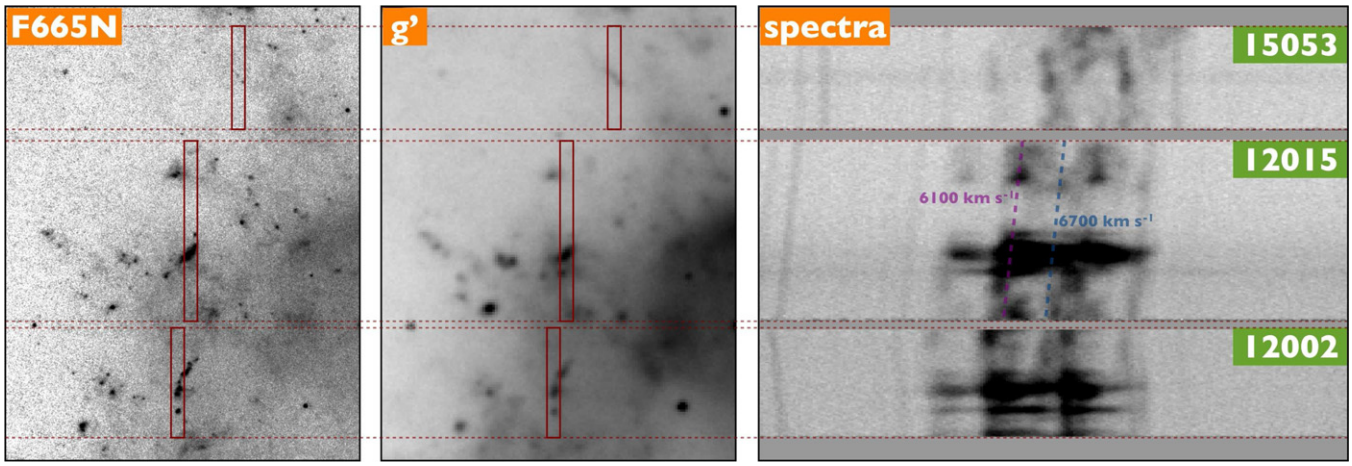

Figure 5. Two-dimensional spectroscopy of the three brightest broad-line emitters, found in three consecutive slits in the shock region. The three panels share the same vertical spatial axis, while the third panel replaces the shared *x*-axis with a dispersion (wavelength) axis. On the left we show the *HST*-Hα image on which the knots were selected, while the center panel shows the GMOS-N *g*-band pre-image, which is more sensitive to diffuse emission features in the background. Such features are seen in the spectra (right; Hα bracketed by [N II]), revealing the presence of a faint, underlying emission component. This will be examined in future work, as in this paper we focus on the knots themselves, and the multiple clumps into which they can be decomposed. As an indication of this substructure we mark two Hα features that register at velocities spanning the full range of redshifts seen in the Quintet, apart from the intruder.

(A color version of this figure is available in the online journal.)

that in this case match the header information in the FITS files. Additionally, we store the right ascension and declination of each target, and save a description of the data set itself as a set of top-level attributes. This format provides much faster `i/o` than FITS (plus better compression for large data sets) and full integration with programming languages popular among astronomers.[13]

[13] HDF5 can be accessed on Python via `h5py` and `PyTables`, IDL via the Exelis IDL HDF5 Library, R via `ncdf4`, Java via `JHI5`, Julia via `HDF5.jl`, and more.

Table 2
Positional Information and Derived Properties of All Observed Targets

ID	α, δ (h m s) ($^\odot$ ′ ″)	Type	u(Hα) (km s^{-1})	σ(Hα) (km s^{-1})	A_V (mag)	SFR ($\times 10^{-3}\ M_\odot\ \mathrm{yr}^{-1}$)	M^* ($\times 10^6\ M_\odot$)	$L_{\mathrm{H}\alpha}$ ($L_{30\,\mathrm{Dor}}$)
10006	22 35 59.196 +33 57 33.98	E	5668	49	0.66	27.5	2.9	0.65
11002	22 36 00.185 +33 57 52.52	E	5764	48	0.98	5.3	2.8	0.10
12002	22 36 00.043 +33 58 06.74	E*	...	...	...	...	...	...
12004	22 35 59.890 +33 58 26.76	E	6020	44	1.04	2.3	2.0	0.04
12005	22 35 59.126 +33 58 36.24	E	6049	44	0.70	2.0	3.3	0.05
12010	22 36 00.550 +33 57 56.66	E	5838	44	0.72	2.0	2.2	0.05
12013	22 35 58.392 +33 57 31.73	E	5647	46	0.70	1.9	2.5	0.05
12014	22 35 55.346 +33 57 11.79	E	5766	49	0.32	1.5	6.1	0.05
12015	22 36 00.094 +33 57 58.82	E*	...	...	...	...	...	...
12018	22 36 00.029 +33 57 46.49	A/E	...	...	...	...	...	...
13001	22 35 59.309 +33 58 15.08	A/E	...	...	...	...	...	...
13003	22 35 59.930 +33 57 47.36	E	5762	48	0.23	1.1	5.6	0.04
13006	22 35 57.658 +33 57 35.22	E	5610	55	1.08	0.5	...	0.01
13011	22 35 59.803 +33 58 08.53	E	6665	89	...	...	...	...
14002	22 35 58.788 +33 58 32.09	A/E	...	...	...	...	...	...
14006	22 35 59.532 +33 58 32.80	E	6023	47	0.82	1.0	2.3	0.02
14030	22 36 00.653 +33 58 07.16	A/E	...	...	...	...	...	...
15053	22 35 59.856 +33 58 20.69	E*	...	...	...	...	...	...
15057	22 35 59.798 +33 58 16.73	A/E	...	...	...	...	...	...
20001	22 36 01.219 +33 58 22.61	E*	...	...	...	...	...	...
20002	22 36 02.150 +33 58 25.64	E*	...	...	...	...	...	...
30093	22 35 58.658 +33 57 43.95	A/E	...	...	...	...	...	...
30109	22 35 58.910 +33 58 49.92	E	6659	59	1.25	20.2	2.1	0.33
30112	22 35 58.008 +33 58 59.71	E	5989	44	0.40	2.4	4.7	0.07
30113	22 35 59.138 +33 59 00.20	E	6858	42	1.94	1.3	1.3	0.01
30115	22 35 57.862 +33 59 11.68	E	5988	51	0.72	0.5	3.9	0.01
30116	22 36 07.567 +33 59 21.37	A/E	...	...	...	...	...	...
30139	22 35 59.256 +33 59 06.02	E	6030	47	0.72	1.9	4.1	0.04
30162	22 35 59.798 +33 57 39.35	E	5710	47	0.95	1.0	2.2	0.02
30170	22 35 54.384 +33 57 17.02	E	5778	45	...	...		...
30174	22 35 59.194 +33 58 47.04	E	6649	45	2.26	7.1	0.8	0.05
50001	22 35 58.068 +33 56 45.48	E	5687	42	1.44	0.4	...	0.01
50003	22 35 56.282 +33 56 53.37	E	5634	55	3.26	1.3	...	0.01
50006	22 35 56.366 +33 57 07.48	E	5670	47	0.59	0.6	4.8	0.02
50007	22 35 58.157 +33 57 09.65	E	5645	44	...	0.1	...	0.01
50009	22 35 56.501 +33 57 19.57	E	5695	52	2.51	1.1	...	0.01
60003	22 35 56.597 +33 58 16.35	A/E	...	...	...	...	...	...
60006	22 35 57.485 +33 58 38.16	E	5998	45	1.35	1.5	2.2	0.02
60011	22 35 58.284 +33 58 48.17	E	6000	46	...	0.8	...	0.03

Notes. "E" and "A" in the "Type" column stand for emission and absorption, and "*" denotes broad-line emission, defined as being broader than the instrumental resolution of ≈2 Å, or 45 km s^{-1}at Hα. Velocity dispersions are deconvolved with the instrumental signature. The faint knot 13011 may be a broad-line emitter. "A/E" sources do not allow for spectral fitting, while the kinematical structure of E* clumps is listed in Table 4. A_V measurements were not possible for sources with low signal in the Hβ region. The columns following the first vertical separator only apply to H II regions. Hα-to-SFR conversions are based on Kennicutt (1998). The final column lists the Hα luminosity normalized to nearby starburst region 30 Dor.

The resulting spectral resolution is approximately 40 km s^{-1} (2.0 Å) and the spectral coverage typically runs from Hβ to [S II]. The exact spectral range shifts as a function of offset from the major axis of observation, a line that runs north–south across the Quintet shock region. We record signal-to-noise ratio (S/N) values of >50 for emission lines (minimum of 5–10 for the faint [O I] 6300 line), while continuum registers at S/N ≈ 10. We will outline measurements in the following section, and discuss results in Sections 4 and 5. The positions of all targets observed and successfully extracted are listed in Table 2, along with measurements and derived information that will be explained in the following sections.

Figure 6 shows the Hα region of all spectra of compact sources. Most (27) appear H II region-like, with the exception of five knots that exhibit emission lines broadened to the point of blending with neighboring spectral features. Four broad-line emitters are shown here, as the fifth was not bright enough for a successful extraction. The occasionally complex velocity–space structure is evident in right panel of Figure 5. Additionally, we show the flux-calibrated spectrum of NGC 7318A in Figure 7, the first to be published of this system. The lack of emission lines confirms it as an early-type galaxy, as morphologically classified by Sulentic et al. (2001). This indicates that the dust features seen across the face of this galaxy are in fact part of NGC 7318B, back-lit by NGC 7318A (see Keel et al. 2013, for examples of this process). The other two galaxies covered show no surprising traits: the Seyfert signature is evident in the bright lines emerging from the nuclear region of NGC 7319 (also shown on Figure 7), along with blue and red "shoulders" on the nebular lines indicative of out-flowing material (as noted by Aoki et al. 1998). NGC 7317 shows no features unexpected from its classification as an elliptical galaxy.

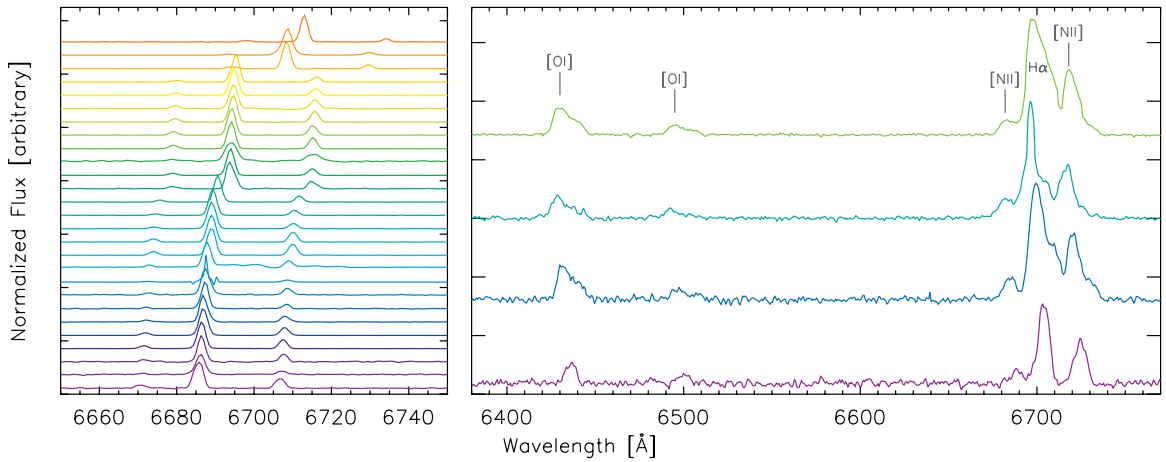

Figure 6. Normalized spectra of H II regions (left) and broad-line knots (right) in Stephan's Quintet, with differently stretched wavelength axes. We exclude eight featureless spectra of stellar associations currently emerging from their cocoons of natal gas. The plots are focused on the spectral region about the Hα and [N II] lines, plus the [O I] 6300, 6340 lines for broad-line spectra. The H II regions are ordered in increasing redshift to reveal various layers of star-forming material along our line of sight. A shallow velocity gradient is evident in the bottom half of this plot, representing knots in the SDR and the lower arc of the shock region, which coincide with the velocity of the intruder, NGC 7318B. The upper half of the left panel is populated mostly by knots in SQ-A, including the top spectrum, at a redshift accordant with a recently discovered CO feature (Guillard et al. 2012). The two spectra below the top are in the systemic velocity of the IGM. Narrow-line emitters will be studied in Section 4. The broad-line spectra are presented in order of increasing flux (bottom to top). These broad, irregular spectral profiles will be examined in Section 3.3 and Figure 8. All spectra are provided as supplemental materials.

(A color version of this figure is available in the online journal.)

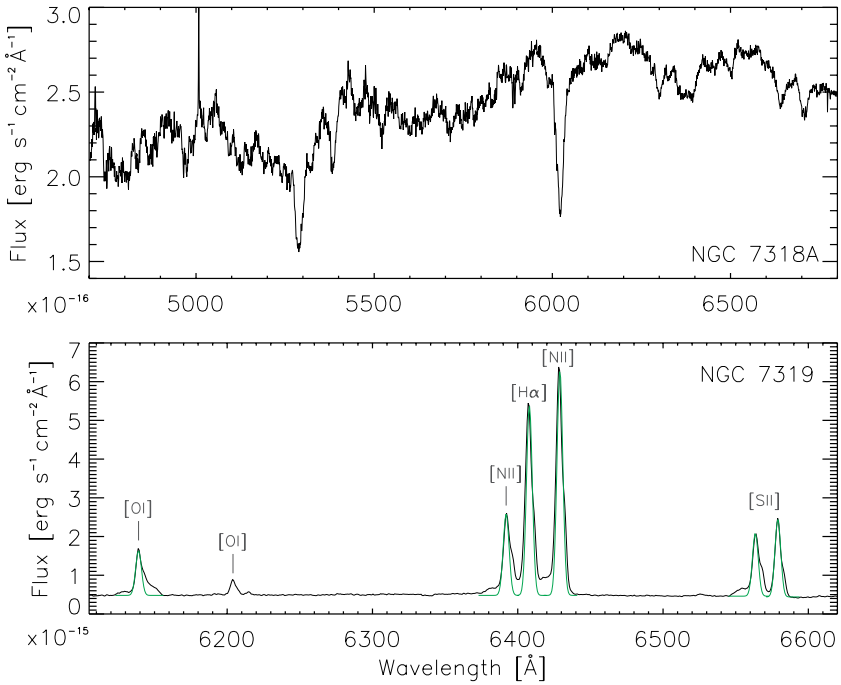

Figure 7. Flux-calibrated spectra of NGC 7318A (top) and NGC 7319 (bottom). There is no trace of emission-line structure in NGC 7318A, branding this galaxy as early type. The 5007 Å sky line has not been entirely subtracted due to the small available sky window in the slit (the observing program was designed for compact sources). NGC 7319 shows no line broadening, consistent with its Seyfert 2 classification, but does feature blue and red shoulders on nebular lines, most prominently [O I] 6400, and the bluer halves of the [N II] and [S II] doublets. We have drawn rough Gaussian fits representing the instrumental resolution at the marked lines. All spectra are provided as supplemental materials.

(A color version of this figure is available in the online journal.)

3. SAMPLE DEFINITION AND SPECTRAL LINE FITTING

3.1. Sample Completeness

Since our spectroscopic slits sample discrete regions across the Quintet, we use the catalog of Fedotov et al. (2011), which reaches fainter sources with imaging, to estimate the completeness of our sample. More specifically, we make use of new spectral energy distribution fitting of *HST*-based *UBVI* photometry, an extension to their star cluster catalog (K. Fedotov et al., in preparation), which includes derivations of age and mass for each source. Given the 20 times poorer resolution of our ground-based spectroscopy, we draw the slit extraction windows on *HST*-images and simply count the number of Fedotov et al. sources that fall within these windows. Since Hα emission was a prerequisite for the selection of our sample, we consider only those sources in the Fedotov et al. catalog younger than 10 Myr.

We estimate that our Hα-emitters represent approximately 9.6% and 13.6% by number of all H II regions in the shock region and SQ-A, respectively. Elsewhere the coverage is low (≈2.5% overall), owing to the sparsity of the SDR and other regions, and the more dense coverage of the shock region and SQ-A in our slit masks. Due to the nature of the observations (spectroscopy versus imaging), our sample is biased toward the most luminous (massive) H II regions. A more extensive, quantitative comparison of the two samples will be presented in K. Fedotov et al. (in preparation).

3.2. Measurement of Radial Velocity, Extinction, and Line Indices

We measured radial velocities of emission-line sources with the `EMSAO` task in the `IRAF-RVSAO` package, and took the Hα velocity to represent each knot (following the Hα-based selection). We then measured the Balmer decrement to derive the reddening of each target through a nominal Hα/Hβ flux ratio of 2.85, and using the extinction laws of Seaton (1979) and Howarth (1983). Kinematical measurements can be found in Table 2. The "A/E" type sources in our sample display a noisy continuum, rather than clear emission or absorption features, hence no measurements were possible. The majority of these appear shaped by a stellar continuum with absorption lines filled, which leads us to assume they are young stellar associations emerging from their natal shrouds (i.e., the remainder of the gas from which the stars formed). In the case of NGC 7318A we employed the `RVSAO-XCSAO` task to cross-correlate its absorption-line spectrum (Figure 7) with four stellar templates from the default library. The velocity was derived as the median of the four values, 6622.5 ± 35.9 km s^{-1}. This uncertainty is computed as the square addition of the individual errors of approximately 18 km s^{-1}. This is consistent with the 6630 ± 23 km s^{-1} literature value of Hickson et al. (1992).

Emission-line strengths were derived through spectral line indices with appropriate continuum windows (Lick indices). We employ `IndexF` (Cardiel 2007) to systematically fit Hβ, [O III], [O I] 6300, Hα, [N II], and [S II] lines across the entire sample (not only emission-line spectra). Hβ and [S II] are not always present due to the distance of some sources from the major axis of observation (as described in Section 2). Line fits are listed in Table 3 and emission-line ratios will be visited in Section 4.2.

3.3. Multi-component Fitting of Broad-line Spectra

Standard methodology, such as that outlined in the previous section, is not appropriate for extracting information from blended spectra. Instead, we used the PAN[14] algorithm and interface to decompose the broad-line regions, those displaying broadening with respect to the instrumental resolution of ≈40 km s^{-1} (cf. typical H II region line widths of 30 km s^{-1}; Fich et al. 1990), into individual emitting knots. This decomposition is shown in Figure 8, and it applies to sources K-12002, K-12015, K-15053, K-20001, and K-20002. We do not plot K-20002, as its spectrum is too faint to trace across the detector. Its broad-line structure is, however, detectable in its two-dimensional spectrum (such as those shown in Figure 5). We also note that the faint K-13011 shows an ambiguous signature that may be interpreted as multi-component or broad emission.

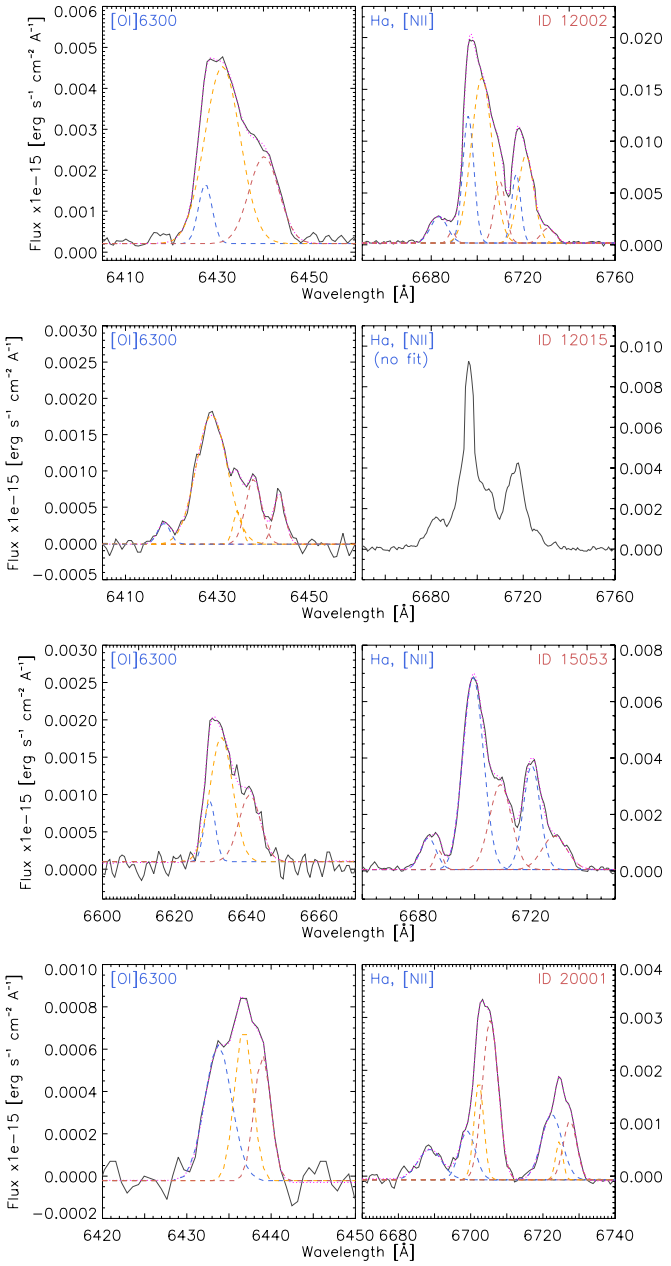

Figure 8. Decomposition of the four broad-line spectra with sufficiently high S/N. A template is constructed based on the [O I] 6300 line before being applied to the Hα/[N II] region. We typically find a three-component fit to provide a reasonable solution, except in the case of K-12015, where four or more subclumps might be present, possibly including a narrow-line feature. The moderate spectral resolution does not allow for further analysis, although we can deduce that all components are broader than the instrumental resolution, and therefore the line widths of regular photoionized Hα (≈30 km s^{-1}); see text.

(A color version of this figure is available in the online journal.)

In order to determine the appropriate number of components for the Hα line we derive a template from [O I] 6300, as it is not subject to contamination from neighboring features. We fit up to four components to the [O I] line, as any additional Gaussians are rejected by the algorithm. We place a 2 Å lower limit to the FWHM of each Gaussian matching the instrumental resolution we measured from sky lines. The results of the kinematical decomposition are listed in Table 4.

[14] Peak analysis; written by Rob Dimeo (NIST) and distributed online at http://www.ncnr.nist.gov/staff/dimeo/panweb/pan.html. A version of the software adapted to astronomy can be found at http://ifs.wikidot.com/pan (Westmoquette et al. 2009).

Table 3
Emission Line Fits with Lick Indices

ID	Hβ λ4860	O III λ4959	O III λ5007	O I λ6300	N II λ6548	Hα λ6563	N II λ6583	S II λ6716	S II λ6731
10006	0.5285 ± 0.0011	0.2676 ± 0.0007	0.7977 ± 0.0019	0.0207 ± 0.0013	0.2010 ± 0.0052	2.0402 ± 0.0167	0.5872 ± 0.0006	0.1804 ± 0.0084	0.1414 ± 0.0035
11001	0.1161 ± 0.0024	0.0253 ± 0.0010	0.0777 ± 0.0011	0.0010 ± 0.0005	0.0414 ± 0.0034	0.6849 ± 0.0034	0.1265 ± 0.0008	0.0327 ± 0.0015	0.0234 ± 0.0009
11002	0.0680 ± 0.0010	0.0174 ± 0.0003	0.0539 ± 0.0002	0.0032 ± 0.0002	0.0345 ± 0.0008	0.3046 ± 0.0055	0.1070 ± 0.0003	0.0413 ± 0.0021	0.0281 ± 0.0019
12002	0.0370 ± 0.0012	0.0087 ± 0.0005	0.0298 ± 0.0010	0.0519 ± 0.0043	0.0359 ± 0.0157	0.2553 ± 0.0180	0.1523 ± 0.0192	0.1221 ± 0.0162	0.0734 ± 0.0122
12004	0.0277 ± 0.0008	0.0089 ± 0.0004	0.0131 ± 0.0011	0.0009 ± 0.0002	0.0170 ± 0.0003	0.1272 ± 0.0027	0.0497 ± 0.0002	0.0175 ± 0.0008	0.0124 ± 0.0003
12005	0.0364 ± 0.0008	0.0316 ± 0.0005	0.1031 ± 0.0001	0.0025 ± 0.0002	0.0093 ± 0.0003	0.1429 ± 0.0009	0.0272 ± 0.0002	0.0145 ± 0.0009	0.0103 ± 0.0004
12010	0.0356 ± 0.0004	0.0178 ± 0.0004	0.0549 ± 0.0004	0.0011 ± 0.0001	0.0109 ± 0.0002	0.1414 ± 0.0016	0.0323 ± 0.0001	0.0160 ± 0.0005	0.0113 ± 0.0003
12013	0.0364 ± 0.0010	0.0135 ± 0.0004	0.0337 ± 0.0006	0.0013 ± 0.0001	0.0157 ± 0.0004	0.1430 ± 0.0024	0.0480 ± 0.0006	0.0176 ± 0.0012	0.0133 ± 0.0009
12014	0.0428 ± 0.0004	0.0277 ± 0.0004	0.0823 ± 0.0006	0.0040 ± 0.0001	0.0090 ± 0.0004	0.1411 ± 0.0015	0.0273 ± 0.0001	...	...
12015	0.0046 ± 0.0007	0.0050 ± 0.0011	0.0041 ± 0.0006	0.0177 ± 0.0014	0.0166 ± 0.0036	0.0806 ± 0.0030	0.0511 ± 0.0039	0.0373 ± 0.0037	0.0253 ± 0.0026
12018	...	−0.0020 ± 0.0003	0.0013 ± 0.0010	−0.0032 ± 0.0004	−0.0001 ± 0.0008	0.0015 ± 0.0005	0.0013 ± 0.0002	−0.0005 ± 0.0006	−0.0001 ± 0.0003
13001	−0.0004 ± 0.0015	−0.0085 ± 0.0003	−0.0004 ± 0.0004	−0.0006 ± 0.0004	−0.0002 ± 0.0001	−0.0003 ± 0.0002	−0.0001 ± 0.0001	0.0011 ± 0.0011	−0.0012 ± 0.0006
13003	0.0370 ± 0.0008	0.0086 ± 0.0003	0.0209 ± 0.0004	0.0016 ± 0.0002	0.0156 ± 0.0003	0.1171 ± 0.0016	0.0490 ± 0.0001	0.0216 ± 0.0006	0.0154 ± 0.0005
13006	0.0059 ± 0.0005	0.0046 ± 0.0003	0.0115 ± 0.0006	0.0002 ± 0.0002	0.0035 ± 0.0002	0.0277 ± 0.0005	0.0099 ± 0.0001	...	...
13011	0.0076 ± 0.0004	−0.0026 ± 0.0002	0.0029 ± 0.0005	0.0012 ± 0.0001	0.0077 ± 0.0022	0.0178 ± 0.0017	0.0032 ± 0.0006	0.0045 ± 0.0007	0.0007 ± 0.0004
14002	−0.0046 ± 0.0029	0.0027 ± 0.0009	0.0044 ± 0.0004	−0.0006 ± 0.0002	−0.0000 ± 0.0004	0.0013 ± 0.0004	0.0022 ± 0.0002	−0.0006 ± 0.0002	0.0000 ± 0.0002
14006	0.0154 ± 0.0012	0.0038 ± 0.0002	0.0215 ± 0.0004	0.0016 ± 0.0002	0.0083 ± 0.0002	0.0639 ± 0.0016	0.0193 ± 0.0002	0.0124 ± 0.0002	0.0060 ± 0.0003
14030	0.0068 ± 0.0005	0.0178 ± 0.0005	0.0165 ± 0.0006	0.0015 ± 0.0001	0.0019 ± 0.0001	0.0172 ± 0.0003	0.0073 ± 0.0003	0.0052 ± 0.0002	0.0036 ± 0.0002
15053	0.0248 ± 0.0012	0.0065 ± 0.0004	0.0156 ± 0.0010	0.0194 ± 0.0022	0.0130 ± 0.0043	0.0774 ± 0.0058	0.0518 ± 0.0046	0.0350 ± 0.0047	0.0226 ± 0.0022
15057	...	0.0039 ± 0.0005	0.0026 ± 0.0004	0.0004 ± 0.0003	0.0000 ± 0.0001	0.0007 ± 0.0001	−0.0002 ± 0.0002	−0.0016 ± 0.0012	−0.0021 ± 0.0006
20001	0.0127 ± 0.0007	−0.0021 ± 0.0004	0.0015 ± 0.0006	0.0060 ± 0.0002	0.0058 ± 0.0020	0.0276 ± 0.0007	0.0149 ± 0.0004	0.0129 ± 0.0006	0.0056 ± 0.0007
20002	...	...	...	0.0007 ± 0.0003	−0.0001 ± 0.0002	−0.0002 ± 0.0003	0.0009 ± 0.0002	0.0055 ± 0.0013	0.0102 ± 0.0024
30093	−0.0675 ± 0.0318	−0.0478 ± 0.0457	−0.0655 ± 0.0191	0.0396 ± 0.0077	−0.0139 ± 0.0045	0.0059 ± 0.0025	−0.0058 ± 0.0060	−0.0269 ± 0.0164	−0.0224 ± 0.0129
30109	0.2050 ± 0.0009	0.1875 ± 0.0009	0.6235 ± 0.0008	0.0107 ± 0.0004	0.0532 ± 0.0457	1.0383 ± 0.0032	0.1117 ± 0.0023	0.0611 ± 0.0042	0.0382 ± 0.0044
30112	0.0631 ± 0.0012	0.0417 ± 0.0015	0.1244 ± 0.0005	0.0018 ± 0.0003	0.0175 ± 0.0003	0.2158 ± 0.0023	0.0546 ± 0.0002	...	...
30113	0.0055 ± 0.0014	0.0153 ± 0.0003	0.0347 ± 0.0004	0.0007 ± 0.0002	0.0023 ± 0.0002	0.0383 ± 0.0002	0.0044 ± 0.0002	0.0015 ± 0.0003	0.0018 ± 0.0001
30115	0.0084 ± 0.0004	0.0066 ± 0.0004	0.0122 ± 0.0004	0.0002 ± 0.0002	0.0028 ± 0.0002	0.0333 ± 0.0004	0.0094 ± 0.0001	...	...
30116	...	...	...	0.0010 ± 0.0004	0.0003 ± 0.0001	−0.0002 ± 0.0001	0.0000 ± 0.0003	−0.0000 ± 0.0001	0.0002 ± 0.0002
30139	0.0339 ± 0.0016	0.0251 ± 0.0011	0.0662 ± 0.0005	0.0031 ± 0.0002	0.0114 ± 0.0018	0.1344 ± 0.0014	0.0345 ± 0.0002	0.0206 ± 0.0018	0.0141 ± 0.0010
30162	0.0167 ± 0.0006	0.0072 ± 0.0004	0.0216 ± 0.0006	0.0008 ± 0.0010	0.0056 ± 0.0011	0.0738 ± 0.0040	0.0317 ± 0.0025	0.0086 ± 0.0020	0.0096 ± 0.0013
30170	0.0408 ± 0.0015	0.0395 ± 0.0002	0.1088 ± 0.0002	0.0034 ± 0.0006	...	...	...	...	...
30174	0.0202 ± 0.0010	0.0221 ± 0.0002	0.0683 ± 0.0003	0.0020 ± 0.0003	0.0156 ± 0.0018	0.1629 ± 0.0024	0.0235 ± 0.0009	0.0133 ± 0.0010	0.0087 ± 0.0005
50001	0.0034 ± 0.0007	−0.0021 ± 0.0003	0.0052 ± 0.0002	0.0010 ± 0.0002	0.0011 ± 0.0001	0.0188 ± 0.0001	0.0033 ± 0.0000	0.0022 ± 0.0001	0.0017 ± 0.0002
50003	0.0011 ± 0.0006	0.0042 ± 0.0007	0.0158 ± 0.0003	−0.0004 ± 0.0003	0.0008 ± 0.0001	0.0141 ± 0.0001	0.0028 ± 0.0000	...	...
50006	0.0133 ± 0.0009	0.0064 ± 0.0003	0.0243 ± 0.0003	0.0027 ± 0.0001	0.0049 ± 0.0002	0.0498 ± 0.0007	0.0113 ± 0.0001	...	...
50007	−0.0010 ± 0.0015	0.0038 ± 0.0006	0.0031 ± 0.0006	0.0004 ± 0.0003	0.0014 ± 0.0002	0.0141 ± 0.0003	0.0039 ± 0.0001	0.0038 ± 0.0001	0.0019 ± 0.0001
50009	0.0025 ± 0.0004	0.0033 ± 0.0003	0.0124 ± 0.0004	0.0001 ± 0.0002	0.0020 ± 0.0001	0.0226 ± 0.0002	0.0064 ± 0.0002	...	...
60003	0.0034 ± 0.0010	−0.0009 ± 0.0004	0.0007 ± 0.0005	0.0004 ± 0.0003	−0.0000 ± 0.0001	−0.0007 ± 0.0001	−0.0002 ± 0.0002	−0.0006 ± 0.0002	−0.0002 ± 0.0001
60006	0.0122 ± 0.0007	0.0029 ± 0.0009	0.0102 ± 0.0005	0.0011 ± 0.0001	0.0089 ± 0.0003	0.0647 ± 0.0010	0.0250 ± 0.0002	...	...
60011	0.0333 ± 0.0004	0.0090 ± 0.0003	0.0210 ± 0.0010	0.0019 ± 0.0002	0.0116 ± 0.0006	0.0926 ± 0.0007	0.0328 ± 0.0000	0.0180 ± 0.0001	0.0114 ± 0.0003

Note. Integrated line fluxes are in units of erg s^{-1} cm^{-2} and have been multiplied by a factor of 10^{15}.

Table 4
Kinematical Decomposition of Broad-line Spectra

ID	$u_R(1)$	$u_R(2)$	$u_R(3)$	$\sigma(1)$	$\sigma(2)$	$\sigma(3)$
			(Hα line, km s^{-1})			
K-12002	6122	6396	6762	130	244	131
K-12015	...	...	...	...	...	...
K-15053	6259	6716	...	197	211	...
K-20001	6259	6396	6533	120	72	118

All components fit by the PAN algorithm are significantly broader than the instrumental profile, typically ≈5 Å, suggestive of an excitation process other than photoionization. *HST* Hα imaging (see Figure 5) relates these spectral components to discernible sub-structure. The clumps are, in fact, filamentary, but spatially blended in the ground-based imaging and spectroscopy (the typical seeing is 0.″8). Given the positions of these knots in the shock region and "AGN bridge," we expect shocks to be the most likely ionizing mechanism, and we will examine this notion in detail in the following section.

4. SHOCKED GAS AND STAR FORMATION IN STEPHAN'S QUINTET

4.1. Velocity Structure of Hα-emitting Regions

Figure 9 maps the velocity and reddening measurements of all Hα-emitting knots across an right ascension–declination plane representing Stephan's Quintet (north is to the top and east is to the left). We have marked the three galaxies for which we obtained spectra, the SDR, and SQ-A for reference, and the main shock region lies between the two shaded rectangles. We plot only the dominant velocity component of broad-line spectra (as triangles), but omit their extinction in plot. Also, the footprint of each aperture has been exaggerated for illustrative purposes. The velocity map shows significant substructure, with spectra arranged in three phase-space groupings:

1. ≃5600 km s^{-1}, the systemic velocity of the intruder, NGC 7318B. This grouping covers the lower half of the bow structure and the SDR, and hence the majority of Hα-emitting regions projected across the large-scale shock. We note a slight, northward velocity gradient throughout.
2. ≃5800 km s^{-1}, the velocity field of the arc to the east of NGC 7318B. This covers the northern part of the bow structure projected across the shock region and extends north to SQ-A.
3. 6400–6800 km s^{-1}, where we find four clumps: three have velocities consistent with the IGM and the fourth coincides with a CO feature recently discovered by Guillard et al. (2012).

The corresponding extinction measurements show a largely random distribution, with, perhaps a higher overall extinction in SQ-A. This region, however, shows the highest SFR anywhere in the system (Xu et al. 2003), which can account for the higher extinction. Note that several data-points do not feature on this plot, as the corresponding sources have either very low S/N or no coverage in the Hβ region.

4.2. Excitation Properties and Metallicity

The excitation properties of all regions are investigated through comparing two emission-line ratios, [O I]/Hα and [N II]/Hα. We list all line ratios in Table 5, while Figure 10 plots them against two sets of model tracks: the grayscale lines on the left show models of H II region evolution (photoionization tracks; Dopita et al. 2006) with three different ionization parameters (R); while the grid on the right shows a full suite of *MAPPINGS* models (Allen et al. 2008) of shock-plus-progenitor ionization with electron density set to 1 cm^{-3}. The magnetic field strength ranges between [0.001, 100] μG from left to right and data align with very weak magnetic fields. The shock velocity scales from bottom to top between [200, 1000] km s^{-1} in 50 km s^{-1} intervals, but the plotted line ratios are suggestive of shock velocities no greater than 300 km s^{-1}. This is less than half the velocity of the collision, consistent with the estimate by Cluver et al. (2010) for the H_2-emitting shocked IGM (based on the [Ne II]/[Ne III] line ratio). Data-points are region-coded to distinguish between the shock region, SQ-A, and SDR on the left, and the three decomposed broad-line clumps of Section 3.3 on the right (K-12002, K-15053, and K-20001).

The metallicity of both model grids in the ionization diagram is set to that of the Small Magellanic Cloud (SMC; 0.4 × $Z_\odot$), as it is found to provide the best overall fit to the data. This seems to counter the frequent finding of metal-enriched star formation in interacting systems (including certain regions of the Quintet; Trancho et al. 2012), however, it is consistent with the recent results of Iglesias-Páramo et al. (2012), who measure sub-solar values for the debris-borne H II regions in the Quintet. We do find some clumps consistent with solar

Table 5
Emission-line Ratios

ID	$\log \frac{[\mathrm{N\,II}]}{\mathrm{H}\alpha}$	$\log \frac{[\mathrm{O\,I}]}{\mathrm{H}\alpha}$
H II regions		
10006	−1.01	−1.99
11002	−0.95	−1.98
12003	−0.88	−1.86
12004	−0.87	−2.15
12005	−1.19	−1.76
12010	−1.11	−2.11
12013	−0.96	−2.04
12014	−1.20	−1.55
14006	−0.89	−1.60
14030	−0.96	−1.06
30109	−1.29	−1.99
30112	−1.09	−2.08
30113	−1.22	−1.74
30139	−1.07	−1.64
30170	0.00	−4.47
30174	−1.02	−1.91
50001	−1.23	−1.27
50006	−1.01	−1.27
50007	−1.00	−1.55
60006	−0.86	−1.77
60011	−0.90	−1.69
Decomposed clumps		
12002 (1)	−0.36	−0.16
12002 (2)	−0.39	0.03
12002 (3)	−0.52	−0.31
15053 (1)	−0.36	1.42
15053 (2)	−0.35	0.98
20001 (1)	0.23	0.80
20001 (2)	−0.54	0.50
20001 (3)	−0.50	0.57

Note. This table only lists spectra with valid [O I] line measurements.

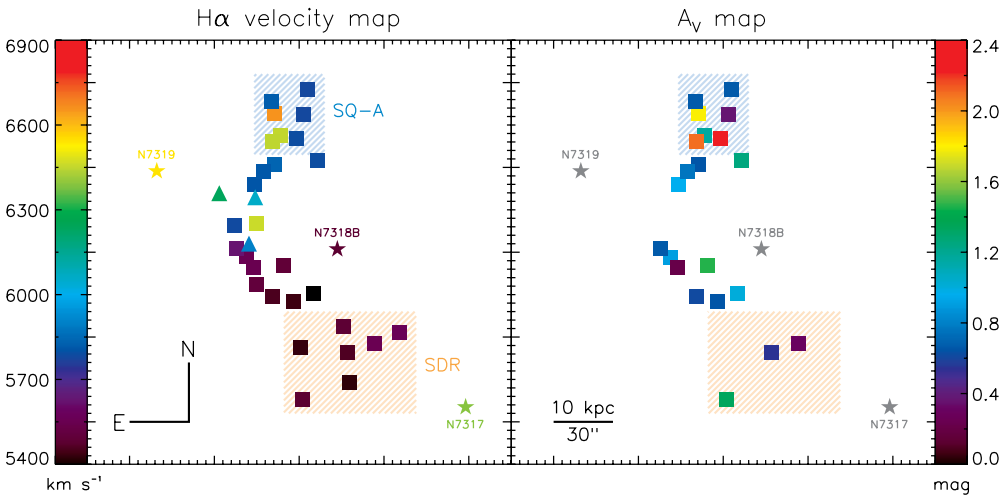

Figure 9. Spatial maps of Stephan's Quintet with measured properties overplotted and color-coded. Left: Hα velocity map of narrow-line Hα-emitters in the Quintet as boxes, broad-line knots as triangles (only the dominant component plotted), and galaxies as stars. The scatter of points in the south represents the SDR, at the velocity of the intruder, NGC 7318B. The arc above is projected across the shock region and displays a northward velocity gradient (see also Figure 6). North of this point a velocity of 5800 km s^{-1} is the norm. Besides these coherent regions, three knots (green boxes, the southernmost may be a broad-line knot) are found at the IGM velocity of ≈6600 km s^{-1}, while one H II region, K-30113 (marked in orange), is found at the high velocity of a recently discovered CO cloud of ≈6860 km s^{-1}(Guillard et al. 2012). Right: reddening map, including only spectra with high S/N in the Hβ spectral region (galaxies plotted for spatial reference). There are no discernible patterns apart from the high-velocity clumps seen through the relatively high extinction column ($A_V > 1.5$ mag) of the SQ-A starburst region.

(A color version of this figure is available in the online journal.)

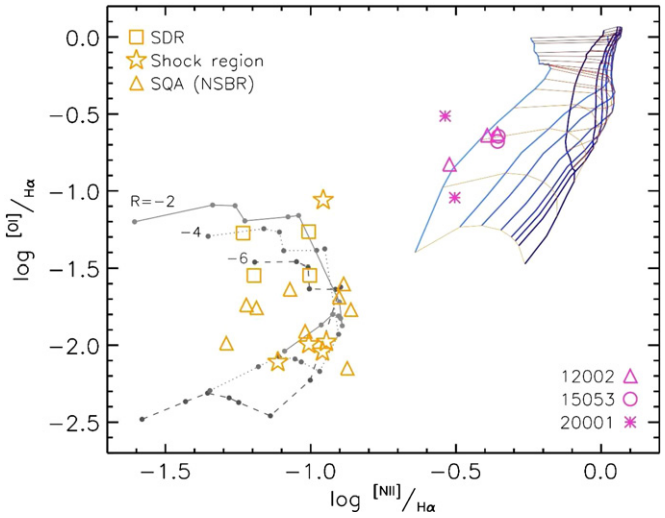

Figure 10. Ionization diagnostics. Orange symbols on the left-hand side mark H II region-like spectra, while magenta symbols on the right mark the decomposed broad-line spectra described in Section 3.3. Gray lines mark models of H II region evolution from Dopita et al. (2006), with SMC metallicity (0.4 × $Z_\odot$). The ionization parameter decreases from top to bottom, while time increases clockwise between 0.1 and 6 Myr. The grid on the top right shows a *MAPPINGS* (Allen et al. 2008) shock-plus-progenitor model grid of SMC metallicity (0.4 × $Z_\odot$) and an electron density of 1 cm^{-3}, the combination of parameters found to best fit the data-points. Magnetic field strength increases from left to right, $-3 < \log(B/\mu G) < 2$ in irregular increments, while the shock velocity ranges between 200 and 1000 km s^{-1} in 50 km s^{-1} steps. The distinction between H II regions and shocked gas is rather striking and points to a different nature for broad- and narrow-line spectra, rather than a superposition of elements across a continuum of velocities.

(A color version of this figure is available in the online journal.)

metallicity, while the high-velocity clump K-30109 appears to have a lower abundance, perhaps at the 0.2 $Z_\odot$ level. Lacking strong metallicity tracers, such as the [O II] 3727 line, we cannot confirm the metallicity as tentatively deduced from Figure 10. A secondary, but unfortunately no more accurate, measure of metallicity is the Kobulnicky & Kewley (2004) parameterization of the [N II]/Hα ratio. Assuming a low ionization parameter, q, following the low electron density, this ratio presents a consistent image of low metallicity throughout the system, with the same few outliers at solar and fifth-solar abundance levels.

4.3. Star Formation Across the Quintet

Some of the most interesting past findings on the Quintet are those treating the baryon budget within this system. For example, there is more mass locked in a cool, molecular phase than neutral H I (Cluver et al. 2010). In order to take a step closer to completing our understanding of this budget we investigate the rate and efficiency of star formation among our sample of H II regions. The extinction-corrected flux of the Hα line can be used to derive the SFR of each knot. We disregard sources with low Hβ flux and hence uncertain A_V derivations (see Section 3.2), convert extinction-corrected Hα fluxes to luminosities through the inverse-square law (using $d = 94$ Mpc for consistency with previous work, e.g., Guillard et al. 2012), and use the Kennicutt (1998) prescription to convert luminosity to an SFR through the relation

$$\mathrm{SFR}\ (M_\odot \mathrm{yr}^{-1}) = 7.9 \times 10^{-42} L_{\mathrm{H}\alpha}(\mathrm{erg\ s}^{-1}).$$

We note that Hα luminosities alone will not account for star formation activity within an H II region in its entirety, owing to the geometry-dependent obscuration. Lacking high-resolution infrared imaging we are unable to apply a correction for obscuration, meaning that our SFR derivations slightly underrepresent the true rates. The total resulting SFR in the 24 qualifying H II regions amounts to 0.084 $M_\odot$ yr^{-1}, more than half of which is found in the two brightest star-forming regions, K-10006 (at the southern edge of the shock region) and K-30109 (the central source in SQ-A). As described in Section 3.1, our sample is biased toward the most luminous (massive) H II regions in Stephan's Quintet. It is therefore not advisable to extrapolate SFR values over the entirety of the

shock region or SQ-A. We can, however, contrast the SFR of our sources with the output of star-forming regions in general. In order to place these values in the context of regular star-forming regions we perform two tests.

First we compare to nearby star-forming regions. For this we need to note that our spectra represent light extracted over 0.75 arcsec^2 to reflect typical seeing, although most knots are intrinsically smaller. At the 94 Mpc distance to the Quintet, that is a physical diameter of ≈450 pc, comparable to large star-forming regions in nearby galaxies—e.g., the giant H II regions NGC 604 ($d \approx 270$ pc; Maíz-Apellániz et al. 2004) and especially 30 Dor ($d \approx 300$ pc; Evans et al. 2011), which is often used as the local benchmark for dense regions of intense star formation activity. Comparing the Hα luminosities of our knots directly with 30 Dor we find none to register the same order of magnitude. For the two brightest knots, K-10006 and K-30109, we record luminosities of 0.65 and 0.33 in 30 Dor units, however, the majority of knots register between 0.01–0.10. This comparison indicates that, apart from the two brightest knots, we are looking at unremarkable star-forming regions and complexes.

For the second test we use the H_2 mass measurements of Guillard et al. (2012) to place our median H II regions on the Bigiel et al. (2008) formulation of the Schmidt–Kennicutt relation (the "star formation law"). We employ the approximation of a uniform H_2 distribution across the Guillard et al. IRAM 30 m telescope beams and establish a median H_2 mass per velocity component of $5 \times 10^8\,M_\odot$, over a beam area of 547 arcsec^2. We therefore estimate an H_2 surface density of $6.9 \times 10^5\,M_\odot$ per slit (0.75 arcsec^2 or 0.12 kpc^2), which translates to $\log(\Sigma_{H2}) = 0.77\,M_\odot\ \mathrm{pc}^{-2}$. The typical SFR among our sample, which, owing to the spectroscopic selection represents the brighter end of the luminosity function, is $10^{-3}\ M_\odot\ \mathrm{yr}^{-1}$, or $\log(\Sigma_{SFR}) = -2.07\ M_\odot \mathrm{yr}^{-1}\ \mathrm{kpc}^{-2}$, and these two values place the average Hα-emitter slightly above the main locus of the Bigiel et al. (2008) data-points, at a SFE of 10%. Considering that 20% is considered an upper limit (e.g., Murray 2011), this is relatively high compared to regular star-forming regions in nearby galaxies. Note, however, that the uncertainty of the uniform approximation may shift the data-point to higher H_2 content, and therefore on or below the locus (as the SFR measurement remains fixed). Lacking spatial information on the CO beams, it is not possible to assess the efficiency of the brightest Hα-emitters in our sample, as the approximation should not be expected to hold.

5. SHOCK-SUPPRESSION, CO COOLING, AND STAR FORMATION

The results presented so far have split the Hα-emitting regions into two classes: regular H II regions, and clumpy filaments of shocked molecular gas. Having derived the kinematical structure, ionization characteristics, metallicity and extinction distributions of all Hα emitters, along with SFRs and masses for the H II regions, we can now assess the role of shocks in affecting the star formation process in Stephan's Quintet.

Given the complex nature of the IGM the two classes of Hα-emitters need to be placed in the context of the multi-phase gas. To facilitate this comparison, we present in Figure 11 the velocity distribution of cool molecular gas, diagnosed through the CO(1–0) line in five pointings, from Guillard et al. (2012). To this we have superposed the velocities of all spatially coincident Hα-emitters.

From this it is evident that the shocked filaments span a large range in redshift, inconsistent with the frame of reference of the intruder. The shock velocities derived for these filaments agree with those for the shock-wide H_2 emission, which we know to be the dominant emission component (Appleton et al. 2006; Cluver et al. 2010). It is therefore reasonable to associate the broad-line emitters with the warm H_2 emission. The typically smaller velocity they display than the IGM indicates deceleration from the oncoming shock front, consistent with the turbulent dissipation of kinetic energy modeled by Guillard et al. (2012).

The kinematics of the H II regions suggest a different distribution in three-dimensional space than the warm molecular filaments. While in SQ-A they appear associated with both the intruder and IGM velocity brackets, across the shock region they are found exclusively in the frame of reference of the intruder. The only possible exception, an H II region in the shocked IGM, is K-13011, a faint, highly extinguished and compact source of ambiguous nature—its S/N does not allow for line decomposition and it is likely to be shock-broadened. Based solely on high-confidence detections, our conclusion is that high-mass star formation is entirely inhibited by the shocks throughout the IGM of Stephan's Quintet. Since our observations do not cover low-mass H II regions, however, it is possible that star formation may proceed at lower levels, undetected by our observing campaign.

Overall, the kinematics of the H II regions projected against the shock and their relatively low masses indicate that they are part of the leading spiral arm of the intruder, or perhaps a tidally induced outer edge pileup, akin to those arising in the dynamical models of Struck & Smith (2012). The slight, northward velocity gradient strengthens this scenario, as it can be attributed to the (assumed prograde) rotating motion of the galaxy. In addition, the considerable reddening (median >1 mag) of the star-forming regions indicates that we may be peering at them through a volume of intra-group material. This interpretation is consistent with the slight spatial mismatch between polycyclic aromatic hydrocarbon (PAH) features and X-ray emission, as discovered by Cluver et al. (2010). The sharp boundary seen in Figure 11 between CO in the intruder and the red lines indicating shocked clumps suggests that the material within the intruder has not been subjected to heating in the same way as the IGM has. The lopsided distribution of Hα emitters in the intruder might indicate that a starburst has yet to occur, as might be expected from the timescale of this interaction—cf. the interacting pairs of Scudder et al. (2012), where the SFR peak often occurs as an interactor travels toward apogalacticon.

The marked difference between the main shock region and SQ-A, where star formation does not appear to be inhibited, is likely due to the longer period over which SQ-A has been forming stars. The previous generation of interaction events sparked the current starburst in this locale, as testified by the ages of star clusters (Fedotov et al. 2011), which are not restricted the embedded phase ($\tau_{age} \lesssim 10$ Myr). Cluver et al. (2010) and Guillard et al. (2012) find comparable masses of warm and cool molecular gas in SQ-A, implying not that the gas was never heated, but that the star formation process was well underway when the shock propagated through the medium some time in the past 10 Myr (or perhaps that the dissipation timescale is shorter in SQ-A; Guillard et al. 2009, 2012).

Finally, it is worthwhile considering Stephan's Quintet in the context of its projected evolution into a set of early-type galaxies with a bright X-ray halo. This will place it in Sequence

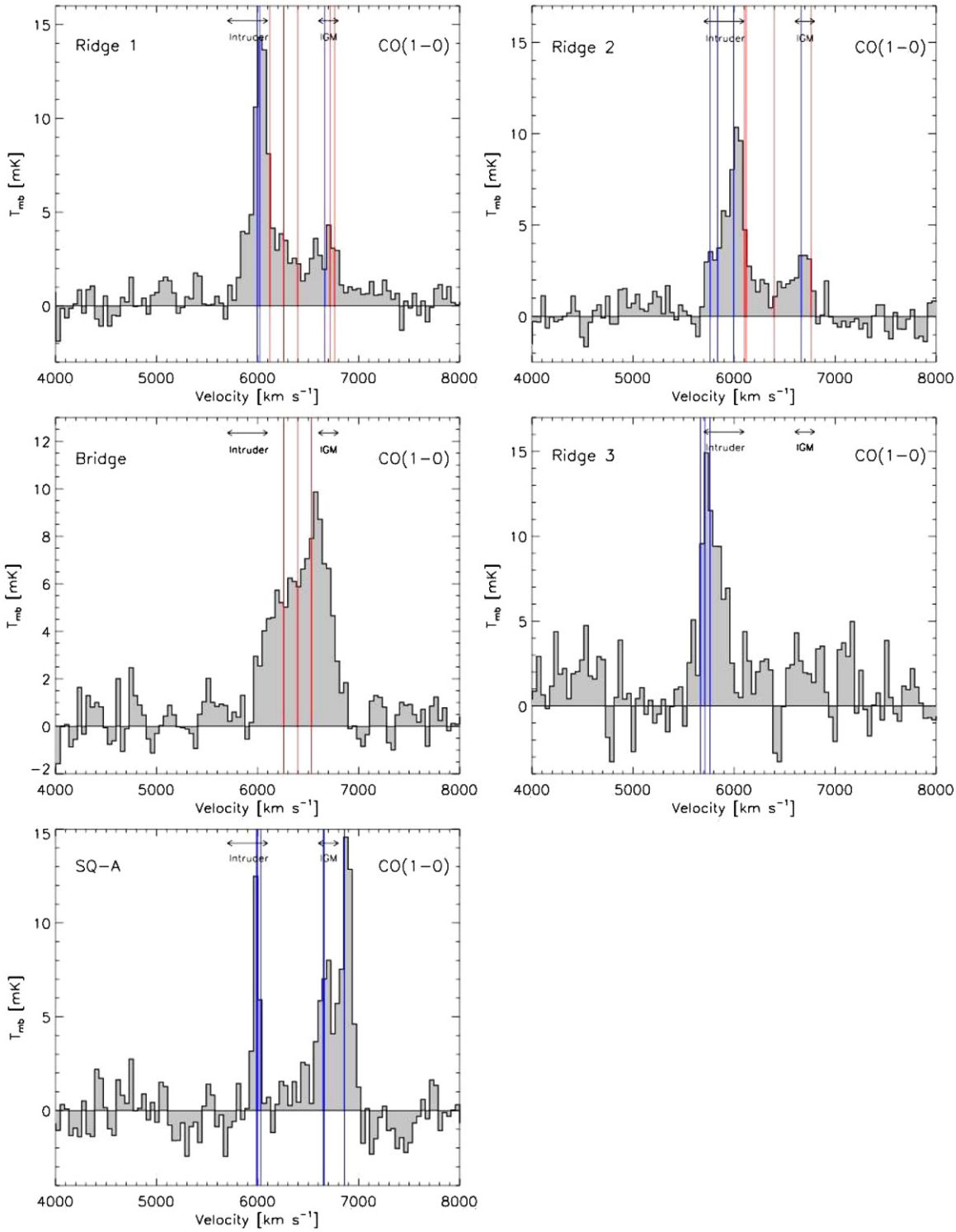

Figure 11. Velocity diagrams of molecular gas from Guillard et al. (2012, as indicated in Figure 1), with those Hα-emitters within 40% of each CO beam-width indicated as blue and red lines for H II regions and shocked clumps, respectively. Ridges 1, 2, and 3 cover the shock region in three consecutive, north-to-south pointings. The slight overlap between Ridges 1 and 2 leads to the duplication of some red lines. The shocked clumps in the "AGN bridge," corresponding to the decomposed knots in K-20001, line up with the observed CO emission but not the IGM, nor the intruder. The majority of H II regions are aligned with the intruder and also match the high-velocity CO clouds projected against SQ-A. In Ridges 1 and 2, which coincide with the peak of X-ray emission, we see a mix of H II regions and shocked filaments in the IGM velocity, but not in the intruder, where there is only star formation. The sharp boundary between the CO distribution of the intruder and the velocity of shocked clumps indicates that material in NGC 7318B lies behind the shock in our line of sight, and hence able to condense into star-forming regions.

(A color version of this figure is available in the online journal.)

B of the Konstantopoulos et al. (2010) evolutionary diagram, where CGs evolve within a shared IGM. Known examples of this class include HCG 42, whose star formation history displays a striking, abrupt cliff near the 2 Gyr mark (Konstantopoulos et al. 2013). Such a star formation history is perhaps to be expected in the Quintet, although, given the many participants in the Quintet interaction and the multiple ongoing starbursts, the quenching of star formation brought on by this shock might

not be as clear-cut as the situation in HCG 42 (see the clumpy color–color plots of Fedotov et al. 2011).

6. SUMMARY

We have presented an investigation of the interplay between the strong, extended shock in Stephan's Quintet and the formation of new stellar associations across this multi-galaxy system. In order to understand the role of the shock in regulating the star formation process, we used Gemini GMOS-N to obtain high-quality optical spectra of ≈40 Hα-bright clumps across this CG, covering the spectral range between Hβ and [S II]. The sources were selected on *HST* images, giving us the ability to map the excitation in this shock region at an unprecedented level of detail.

The studied Hα emitters display a bimodality in terms of their emission-line widths and ionization parameters. We find a set of five (possibly six) broad-line objects, which we decompose into several (three or four) individual clumps. These sources are filamentary in nature, as evident in Hα imaging from *HST*, and each individual knot exhibits broadening at a multiple of the 40 km s^{-1} resolution element—with the possible exception of a single narrow component in K-12015, which we were unable to decompose. By studying their ionization characteristics, we identify all components that make up these filaments as molecular gas heated by the propagation of a shock front at 100–300 km s^{-1}, consistent with the $H_2$0–0 S(1) emission mapped by Cluver et al. (2010, which traces the X-ray-emitting medium). While these H_2 clumps are significantly cooler than the X-ray-emitting gas that surrounds them, they display no evidence of star formation.

The population of ≈30 H II regions show SFRs and SFR-densities similar to nearby, regular star-forming regions, with the exception of two knots that are more akin to prolific stellar nurseries such as 30 Dor. As a whole, they can be split into three sub-components according to their spatial distribution: those in the SDR, those projected against the shock region, and those being formed in the SQ-A starburst. Kinematically, however, they are more consistent than that. Hα emitters in the SDR and shock region display a mean velocity of ≈5600 km s^{-1} and a slight but uninterrupted velocity gradient. This not only places them in the frame of reference of the intruder, but is consistent with the prograde circular motion of a spiral arm. Further support for this thesis stems from several other pieces of evidence: relatively high reddening, a low median SFR, and a striking accord between the spatial distributions of H II regions and PAH features studied by Cluver et al. (2010, with ≈1″ spatial resolution, similar to our GMOS data), so we associate the star-forming regions with the intruder. Hα-emitters projected against the shock region appear to be situated in a spiral arm of NGC 7318B. Those in the SDR might be associated with an extension of the spiral arm, a debris structure, although the projected spatial separation between NGC 7318B and the boundary of the SDR is substantial. Knots in SQ-A are simple products of an ongoing starburst whose onset pre-dates the galaxy–IGM collision that gave rise to the shock front. These pieces of evidence, along with the slightly higher SQ-A velocity are consistent with the Renaud et al. (2010) and Hwang et al. (2012) models that trace the origin of SQ-A as debris ejected from NGC 7318A before colliding with the IGM. Having associated the entire population of H II regions projected against the shock to the intruder instead, we find no evidence for star formation in the shocked IGM. We therefore conclude that the process is altogether suppressed throughout the hot phase of the clumpy medium.

We find three star-forming regions and one potential broad-line clump outside the above-mentioned phase-space distribution. They are projected across the shock region and SQ-A but lie at higher velocities (6400–6600 km s^{-1}), in accord with systemic velocity of the IGM. One exception, at ≈6800 km s^{-1}, is an optical counterpart to a CO cloud recently discovered by Guillard et al. (2012) and displays a metallicity lower than the average—which is already low at SMC levels. We also present the optical spectrum of NGC 7318A for the first time, and classify it as an early-type galaxy, confirming the morphological classification of Sulentic et al. (1995).

Understanding the effect of strong shocks on the evolution of CG groups is of great importance to the empirical framework of galaxy evolution. The majority of galaxies and stellar mass in the local universe are found in groups (Small et al. 1999; Eke et al. 2005), where high-speed collisions are infrequent, but not rare—especially in CGs (Cluver et al. 2013). The build-up of X-ray haloes in low-mass CGs is conditional on such collisional heating of the IGM, as their shallow potential wells close the conventional channels that dominate in more populous groupings (e.g., the frictional energy exchange between massive galaxies and the rich IGM in clusters; see also Desjardins et al. 2014). In addition, groupings of galaxies at higher redshifts, before matter assembled to its current stage, might have resembled present-day CGs. If the Quintet is an appropriate interpretive guide to the effect of shock-heating, we can deduce that large volumes of molecular gas can be locked in this hot phase for ∼1 Gyr or more at a time, while the group evolves inside an X-ray halo. In that way, the stochastic occurrence of an intruder will define the evolution of a CG—at least the lower branch of the Konstantopoulos et al. (2010) evolutionary pathway where strong interactions between gas-rich galaxies dominate. This must be taken into account in models of galaxy evolution and in compiling the baryon budgets of galaxy groups.

We thank the anonymous referee for helping us reinforce some of the analysis.

Based on observations obtained at the Gemini Observatory (program ID GN-2010B-Q-56), which is operated by the Association of Universities for Research in Astronomy, Inc., under a cooperative agreement with the NSF on behalf of the Gemini partnership: the National Science Foundation (United States), the National Research Council (Canada), CONICYT (Chile), the Australian Research Council (Australia), Ministério da Ciência, Tecnologia e Inovação (Brazil), and Ministerio de Ciencia, Tecnología e Innovación Productiva (Argentina).

Based on observations made with the NASA/ESA *Hubble Space Telescope*, obtained from the data archive at the Space Telescope Science Institute. STScI is operated by the Association of Universities for Research in Astronomy, Inc. under NASA contract NAS 5-26555.

I.S.K. acknowledges support from grant no. 1439092 from the Jet Propulsion Laboratory. I.S.K. is also grateful for the hospitality of the staff at the NASA Herschel Science Center, the Giant Magellan Telescope Organisation, and Carnegie Observatories, all in Pasadena, CA, where much of this work was undertaken.

S.C.G. and K.F. thank the Canadian Natural Science and Engineering Research Council and the Ontario Early Researcher Award Program for support.

REFERENCES

Allen, M. G., Groves, B. A., Dopita, M. A., Sutherland, R. S., & Kewley, L. J. 2008, ApJS, 178, 20
Aoki, K., Kosugi, G., Yoshida, M., Ohtani, H., & Wilson, A. S. 1996, AJ, 111, 140
Appleton, P. N., Guillard, P., Boulanger, F., et al. 2013, ApJ, 777, 66
Appleton, P. N., Xu, K. C., Reach, W., et al. 2006, ApJL, 639, L51
Bigiel, F., Leroy, A., Walter, F., et al. 2008, AJ, 136, 2846
Bonnell, I. A., Dobbs, C. L., & Smith, R. J. 2013, MNRAS, 430, 1790
Cardiel, N. 2007, in Proceedings of the 7th Scientific Meeting of the Spanish Astronomical Society, Vol. 186, Measuring Line-strength Indices in a Systematic Way, ed. J. F. Figueras, J. M. Girart, M. Hernanz, & C. Jordi (Highlights of Spanish Astrophysics IV; Berlin: Springer)
Cluver, M. E., Appleton, P. N., Boulanger, F., et al. 2010, ApJ, 710, 248
Cluver, M. E., Appleton, P. N., Ogle, P., et al. 2013, ApJ, 765, 93
Dale, J. E., Clark, P. C., & Bonnell, I. A. 2007, MNRAS, 377, 535
Desjardins, T. D., Gallagher, S. C., Hornschemeier, A. E., et al. 2014, ApJ, submitted
Dopita, M. A., Fischera, J., Sutherland, R. S., et al. 2006, ApJS, 167, 177
Eke, V. R., Baugh, C. M., Cole, S., et al. 2005, MNRAS, 362, 1233
Elmegreen, B. G. 2002, ApJ, 577, 206
Elmegreen, B. G., & Lada, C. J. 1977, ApJ, 214, 725
Evans, C. J., Taylor, W. D., Hénault-Brunet, V., et al. 2011, A&A, 530, A108
Fedotov, K., Gallagher, S. C., Konstantopoulos, I. S., et al. 2011, AJ, 142, 42
Fich, M., Dahl, G. P., & Treffers, R. R. 1990, AJ, 99, 622
Gallagher, S. C., Charlton, J. C., Hunsberger, S. D., Zaritsky, D., & Whitmore, B. C. 2001, AJ, 122, 163
Gao, Y., & Xu, C. 2000, ApJL, 542, L83
Getman, K. V., Feigelson, E. D., Sicilia-Aguilar, A., et al. 2012, MNRAS, 426, 2917
Guillard, P., Boulanger, F., Pineau Des Forêts, G., & Appleton, P. N. 2009, A&A, 502, 515
Guillard, P., Boulanger, F., Pineau des Forêts, G., et al. 2012, ApJ, 749, 158
Hickson, P., Mendes de Oliveira, C., Huchra, J. P., & Palumbo, G. G. 1992, ApJ, 399, 353
Hopkins, P. F., Quataert, E., & Murray, N. 2011, MNRAS, 417, 950
Howarth, I. D. 1983, MNRAS, 203, 301
Hwang, J.-S., Struck, C., Renaud, F., & Appleton, P. N. 2012, MNRAS, 419, 1780
Iglesias-Páramo, J., López-Martín, L., Vílchez, J. M., Petropoulou, V., & Sulentic, J. W. 2012, A&A, 539, A127
Keel, W. C., Manning, A. M., Holwerda, B. W., et al. 2013, PASP, 125, 2
Kennicutt, R. C., Jr. 1998, ARA&A, 36, 189
Klessen, R. S., & Hennebelle, P. 2010, A&A, 520, A17
Kobulnicky, H. A., & Kewley, L. J. 2004, ApJ, 617, 240
Konstantopoulos, I. S., Gallagher, S. C., Fedotov, K., et al. 2010, ApJ, 723, 197
Konstantopoulos, I. S., Maybhate, A., Charlton, J. C., et al. 2013, ApJ, 770, 114
Leon, S., Combes, F., & Menon, T. K. 1998, A&A, 330, 37
Mac Low, M.-M. 2013, in IAU Symp. 292, Molecular Gas, Dust, and Star Formation, ed. T. Wong & J. Ott (Cambridge: Cambridge Univ. Press), 3
Maíz-Apellániz, J., Pérez, E., & Mas-Hesse, J. M. 2004, AJ, 128, 1196
Murray, N. 2011, ApJ, 729, 133
Nakamura, F., & Li, Z.-Y. 2011, ApJ, 740, 36
Petitpas, G. R., & Taylor, C. L. 2005, ApJ, 633, 138
Renaud, F., Appleton, P. N., & Xu, C. K. 2010, ApJ, 724, 80
Reynaud, D., & Downes, D. 1998, A&A, 337, 671
Schlegel, D. J., Finkbeiner, D. P., & Davis, M. 1998, ApJ, 500, 525
Scudder, J. M., Ellison, S. L., Torrey, P., Patton, D. R., & Mendel, J. T. 2012, MNRAS, 426, 549
Seaton, M. J. 1979, MNRAS, 187, 73
Sellwood, J. A., & Balbus, S. A. 1999, ApJ, 511, 660
Small, T. A., Ma, C.-P., Sargent, W. L. W., & Hamilton, D. 1999, ApJ, 524, 31
Smith, B. J., & Struck, C. 2001, AJ, 121, 710
Struck, C., & Smith, B. J. 2012, MNRAS, 422, 2444
Sulentic, J. W., Pietsch, W., & Arp, H. 1995, A&A, 298, 420
Sulentic, J. W., Rosado, M., Dultzin-Hacyan, D., et al. 2001, AJ, 122, 2993
Tamburro, D., Rix, H.-W., Leroy, A. K., et al. 2009, AJ, 137, 4424
Thompson, T. A., Quataert, E., & Murray, N. 2005, ApJ, 630, 167
Trancho, G., Konstantopoulos, I. S., Bastian, N., et al. 2012, ApJ, 748, 102
Verdes-Montenegro, L., Yun, M. S., Perea, J., del Olmo, A., & Ho, P. T. P. 1998, ApJ, 497, 89
Véron-Cetty, M.-P., & Véron, P. 2006, A&A, 455, 773
Westmoquette, M. S., Exter, K. M., Christensen, L., et al. 2009, arXiv:0905.3054
Xu, C., Sulentic, J. W., & Tuffs, R. 1999, ApJ, 512, 178
Xu, C. K., Iglesias-Páramo, J., Burgarella, D., et al. 2005, ApJL, 619, L95
Xu, C. K., Lu, N., Condon, J. J., Dopita, M., & Tuffs, R. J. 2003, ApJ, 595, 665
Yun, M. S. 1997, ApJL, 425, L21